Editors' Suggestion

Spontaneous Mean Flow Emerging from Electrohydrodynamic Turbulence in Nematic Liquid Crystals

Yuki Sato,[1] Takato Mera,[2] Fumiaki Kobayashi,[3] Jun Takeda,[4] Koki Yoshihara,[4] Yuji Sasaki,[5] Hiroshi Orihara,[6,*] Tomoyuki Nagaya,[2,6,†] and Jong-Hoon Huh[1,‡]

[1]*Department of Physics and Information Technology, Faculty of Computer Science and Systems Engineering, Kyushu Institute of Technology, Fukuoka 820-8502, Japan*

[2]*Natural Science Program, Graduate School of Engineering, Oita University, Oita 870-1192, Japan*

[3]*Department of Physics, School of Science, Kyushu University, Fukuoka 819-0395, Japan*

[4]*Department of Applied Physics, Graduate School of Engineering, Hokkaido University, Sapporo 060-8628, Japan*

[5]*Faculty of Engineering, Hokkai-Gakuen University, Sapporo 064-0926, Japan*

[6]*Physics Collaboration Program, Faculty of Science and Technology, Oita University, Oita 870-1192, Japan*

(Received 4 June 2026; revised 31 August 2026; accepted 25 September 2026; published 18 November 2026)

Turbulence is commonly regarded as the ultimate state of disorder in which coherent structures do not persist in time averages. Here, we show that fully developed electrohydrodynamic turbulence in nematic liquid crystals instead supports a robust, system-spanning mean flow. Using high-speed imaging and particle tracking, we uncover a persistent large-scale vortex that emerges spontaneously from the dynamic scattering mode-2, a turbulent state studied for over five decades. This mean flow survives temporal averaging and reflects genuine material transport rather than apparent motion of orientational patterns. Three-dimensional nematohydrodynamic simulations reproduce the observed flow and reveal a Poiseuille-like velocity profile with vanishing interfacial shear stress, while two-dimensional modeling captures the coarsening dynamics leading to vortex selection. The emergence of a zero-wave-number flow directly from fully developed turbulence contrasts sharply with previously studied active and classical turbulent systems, where large-scale organization typically arises at finite wavelengths or requires external forcing.

DOI: 10.1103/rh1y-bsjj

Recent rheological measurements reveal that certain nematic liquid crystals (NLCs) exhibit negative apparent viscosity under applied electric fields [1–3]. Similar behavior occurs in other active suspensions [4–8] but is several orders of magnitude larger in liquid crystals. NLCs consist of rodlike molecules that flow like liquids while maintaining collective orientational order. The average molecular orientation is represented by a unit vector $\mathbf{n}$, called the director. The dielectric permittivity and electrical conductivity of NLCs exhibit anisotropy, characterized by $\Delta\varepsilon = \varepsilon_{\parallel} - \varepsilon_{\perp}$ and $\Delta\sigma = \sigma_{\parallel} - \sigma_{\perp}$, respectively, where $\parallel$ and $\perp$ denote directions parallel and perpendicular to $\mathbf{n}$ [9]. Placing NLCs with $\Delta\varepsilon < 0$ and $\Delta\sigma > 0$ between parallel electrodes and applying an electric field induces the formation of periodic roll-convection patterns called Williams domains (WDs) [10–12]. With increasing voltage, the WDs transition through fluctuating WDs, grid patterns, and a dynamic scattering mode-1, ultimately evolving into fully developed turbulence known as dynamic scattering mode-2 (DSM2) [13–16]. Negative apparent viscosity was discovered specifically in the DSM2 state, which arises from continuous electrical energy input [1–3]. This negative viscosity enables spontaneous rotation in a torque-free configuration, where the upper plate of a rheometer is released from external torque under an applied electric field [1–3]. Continuum simulations based on nematohydrodynamics reproduce this behavior, showing that the time-averaged velocity field adopts a simple-shear-like profile in which the velocity gradient vanishes at both confining surfaces [17]. In rheological setups, the free upper plate permits this simple-shear-like flow. However, constraining the upper plate suppresses this flow, raising the question of what alternative mean flow, if any, would emerge instead.

In this Letter, we employ high-resolution optical microscopy combined with particle tracking to directly measure the flow field. A different spontaneous mean flow emerges from that observed in a rheometer under the torque-free configuration, generating a large-scale vortex (LSV) spanning the entire electrode region. Three-dimensional

*Contact author: orihara164a@gmail.com

†Contact author: nagaya@oita-u.ac.jp

‡Contact author: huh.jong-hoon244@mail.kyutech.jp

Published by the American Physical Society under the terms of the Creative Commons Attribution 4.0 International license. Further distribution of this work must maintain attribution to the author(s) and the published article's title, journal citation, and DOI.

simulations, extended to the confined geometry, clarify the velocity profile. Moreover, two-dimensional simulations capture the transient dynamics of LSV formation. Recent studies on active nematics have shown that defect-mediated chaotic flows transiently organize into coherent structures but do not develop a persistent, system-spanning mean flow, even under confinement or self-imposed constraints [18,19]. In sharp contrast, the DSM2 turbulence investigated herein exhibits the emergence of a robust zero-wave-number mean flow directly from a fully developed turbulent state, highlighting a fundamentally distinct route for macroscopic flow organization in nonequilibrium nematic systems.

Despite decades of studies on DSM turbulence [13,14,20–22], time-persistent mean flow has never been reported. To investigate this mean flow and the LSV it generates, the entire active area (1.2×1.2 mm^2) was imaged at 200 frames per second, compared with the 30 frames per second used in most prior studies [13–15]. This captures previously unresolved patterns and dynamic behaviors, enabling detailed analysis of the unexpected properties of mean flow. Transparent indium-tin-oxide electrode cells (KSRP-50, EHC. Co., Ltd., Japan) with planar alignment [$\mathbf{n}_0 = (1, 0, 0)$] were prepared with an NLC layer thickness of $d = 50$ μm. The NLC material was 1-(4-(Pentylphenyl)ethynyl)-4-(4-propylcyclohexyl)carbonyloxy)-2,3-difluorobenzene (PPDFB) with $\Delta\varepsilon < 0$ and $\Delta\sigma > 0$ [3], which was doped with 1.0 wt.% tetrabutylammonium bromide to increase the conductivity of PPDFB and thereby realize the conductive electroconvection regime with lower voltages and wider frequencies [23]. All experiments were conducted at $T = 75$ °C under an ac field $E(t) = \sqrt{2}E\cos(2\pi ft)$ using a standard optical condition for electroconvection with a single polarizer [13–15].

Figure 1(a) shows a typical steady-state turbulence in the DSM2 state under an applied electric field ($f = 100$ Hz). The fine, white-speckled patterns in this image arise from spatial distortions of the director field and specifically reflect the spatial distribution of disclinations [9,13]. The relative positions of the speckles undergo local changes through continuous creation and annihilation of the speckles while drifting collectively in a preferred direction. The drift velocity field was obtained using the matlab-based software PIVLab [24,25], which calculates displacement vectors from the cross-correlation between successive video frames. The recorded images (740×740 pixels) were analyzed using a multipass procedure with interrogation windows of 128×128 and 64×64 pixels and 50% overlap, resulting in velocity fields consisting of 22×22 vectors. Standard vector validation and filtering implemented in PIVLab were applied to remove spurious vectors. The reliability of the particle image velocimetry analysis in the presence of the continuous creation and annihilation of speckles is examined in detail in Supplemental Material (S1) [26]. Figures 1(b) and 1(c) show the velocity $\mathbf{v}$ and

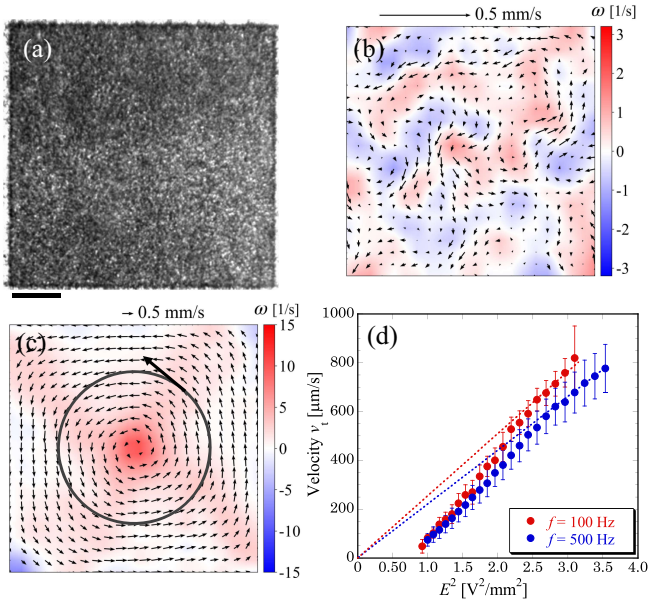


FIG. 1. DSM2 pattern and velocity-vorticity maps. (a) A typical DSM2 pattern at $f = 100$ Hz. Corresponding velocity and vorticity maps at (b) $E = 0.89$ V/μm and (c) $E = 1.4$ V/μm. (d) Electric-field dependence of the mean tangential velocity v_t along the circumference of a circle with a radius of 0.35 mm, as indicated in (c); this dependence was reproduced at a different frequency $f = 500$ Hz. See Supplemental Video1 [26] for the detail of (b). The scale bar in (a) is 200 μm.

associated vorticity field $\boldsymbol{\omega} = \nabla \times \mathbf{v}$ corresponding to DSM2s for $E = 0.89$ V/μm and $E = 1.4$ V/μm, respectively. The velocity fields were obtained by averaging over 21 and 81 frames for Figs. 1(b) and 1(c), respectively. Despite the common presence of a local flow, the two fields exhibit remarkable differences. An LSV spanning the entire electrode area is apparent in Fig. 1(c), which persists after time averaging. In contrast, no LSV appears in Fig. 1(b); instead, the local velocity and vorticity fields fluctuate substantially with time, as shown in Supplemental Video1 [26]. Whether the flow pattern reflects phase-wave-like director motion [27–29] or genuine material transport is addressed below. The tangential velocity v_t along the circumference in Fig. 1(c) rises above a threshold field (e.g., $E \sim 0.95$ V/μm for $f = 100$ Hz) and becomes proportional to E^2 [Fig. 1(d)], consistent with spontaneous shear velocity in torque-free configuration [1–3,17].

LSV formation was examined under fixed conditions ($E = 1.4$ V/μm, $f = 100$ Hz) using time-dependent velocity and vorticity maps computed from 21 successive frames, yielding a velocity field (Fig. 2). Upon application of the electric field, small clockwise (blue, $\omega < 0$) and counterclockwise (red, $\omega > 0$) vortices are generated successively. Their generation is essentially completed by around 0.9 s, after which vortices continue to merge, eventually giving rise to a single LSV; see Supplemental Video2 [26]. The rotation sense of the LSV is determined

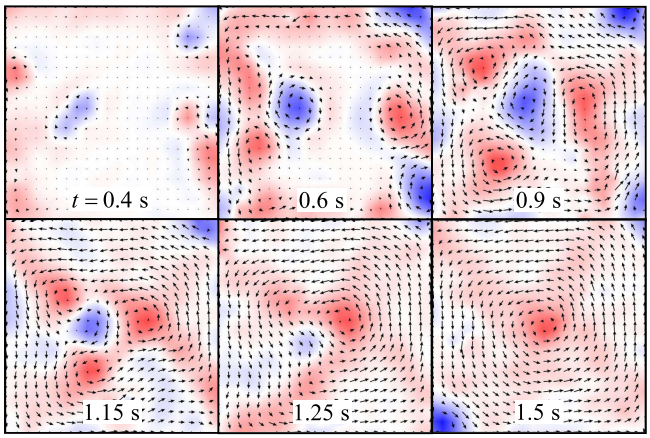


FIG. 2. Time evolution of velocity (arrows) and vorticity (color graduation) fields. To observe the formation of the large-scale vortex (LSV), the voltage was abruptly ramped from $E = 0$ to $E = 1.4$ V/μm ($f = 100$ Hz). A DSM2 pattern appears immediately; for $t > 1.5$ s, LSV persists within DSM2 for the entire observation period, typically exceeding 15 s. See Supplemental Video2 [26] for the details. The vorticity color scale is the same as in Fig. 1(c).

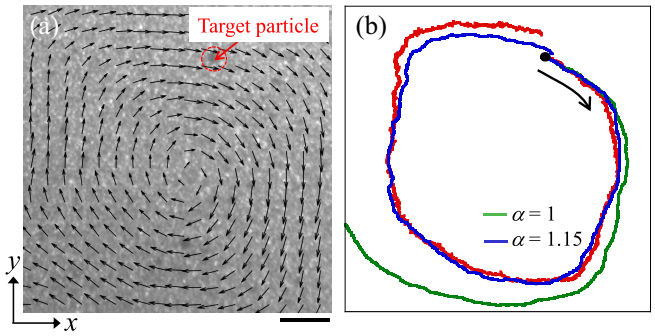


FIG. 3. Particle tracking in DSM2. (a) Snapshot of LSV within DSM2 ($E = 3.0$ V/μm; $f = 100$ Hz) and velocity field. (b) Trajectory of a single microparticle on the flows, observed by a particle tracking method (red line), and trajectories calculated from the velocity field for $\alpha = 1$ (green line) and $\alpha = 1.15$ (blue line). See Supplemental Video3 [26] for the details of (a). The scale bar is 200 μm.

randomly by initial fluctuations. Furthermore, the core of the fully developed LSV settles at the center of the rectangular cell. The vortex persists as long as the applied voltage is maintained.

To determine whether the pattern flow corresponds to the phase-wave-like motion of the director field [27–29] or arises from genuine material transport, spherical polymer microbeads with a diameter of 9.96 ± 0.46 μm (Micropearl SP-210, SEKISUI Chemical Co., Ltd., Japan) introduced into the cell were directly observed. Figure 3(a) shows a frame from the DSM2 state ($E = 3.0$ V/μm, $f = 100$ Hz) together with the velocity field averaged over 20 s. The trajectory of a single particle obtained from the video [Fig. 3(b), red line] follows the streamline of this velocity field, demonstrating that the observed flow pattern originates from genuine material transport rather than a phase-wave-like motion. During the observation interval, the velocity field is nearly steady. Thus, the trajectory could be calculated as $\mathbf{r}(t + \Delta t) = \mathbf{r}(t) + \mathbf{v}(\mathbf{r}(t))\Delta t$, where $\mathbf{r}(t)$ denotes the particle position at t. The calculated trajectory [Fig. 3(b), green line] progressively deviates from the measured trajectory (red line), and the calculated velocity is consistently slower than the actual particle velocity. To account for this discrepancy, the above equation was modified by multiplying the velocity by a factor α. For $\alpha = 1.15$, the resulting trajectory [Fig. 3(b), blue line] agrees well with the experimental trajectory (red line). The fitted value of α exhibits slight variations among different particles (typically $1 < \alpha < 1.4$), which can be attributed to differences in their vertical positions within the cell and in the local boundary conditions, including proximity to the side walls. Indeed, the discrepancy is consistent with a Poiseuille-like mean flow profile, where the flow velocity must vanish at the interfaces with the upper and lower plates [Fig. 4(d)]. If the motion of defects follows such a flow, their velocity would be zero at the interfaces and maximal at the center of the cell. Image processing effectively averages the velocity over the cell thickness, yielding values substantially smaller than those at the cell midplane, where the tracer particles are most likely located in the cell gap.

The experiments confirm that a spontaneous mean flow exists in the DSM2 state when the upper plate is fixed. Because direct measurement of the three-dimensional flow field on the relevant spatial and temporal scales is experimentally inaccessible, a simulation approach from the literature [17] was extended to the present confined geometry. Ideally, such simulations should be performed using the material parameters of PPDFB; however, due to the absence of a complete set of these parameters, a Q-tensor model [30,31], incorporating the material parameters of 4-methoxybenzylidene-4-butylaniline (MBBA) from previous studies [17,32–34], was employed, with the cell gap adjusted to 50 μm. Moreover, the ac frequency (100 Hz) was set to match the present experimental conditions, and the boundary conditions were chosen to be consistent with the experimental setup. The use of the material parameters of MBBA is justified by the fact that PPDFB and MBBA exhibit qualitatively similar rheological characteristics in the negative-viscosity regime despite variations in the magnitude of the effect [3]. In addition, an LSV was also observed in MBBA. However, because of the very low flow velocity, sufficient data on the LSV formation process and microparticle trajectories, as obtained for PPDFB, have not yet been acquired; see Supplemental Material (S5) [26]. These considerations support the use of MBBA material parameters to qualitatively reproduce the

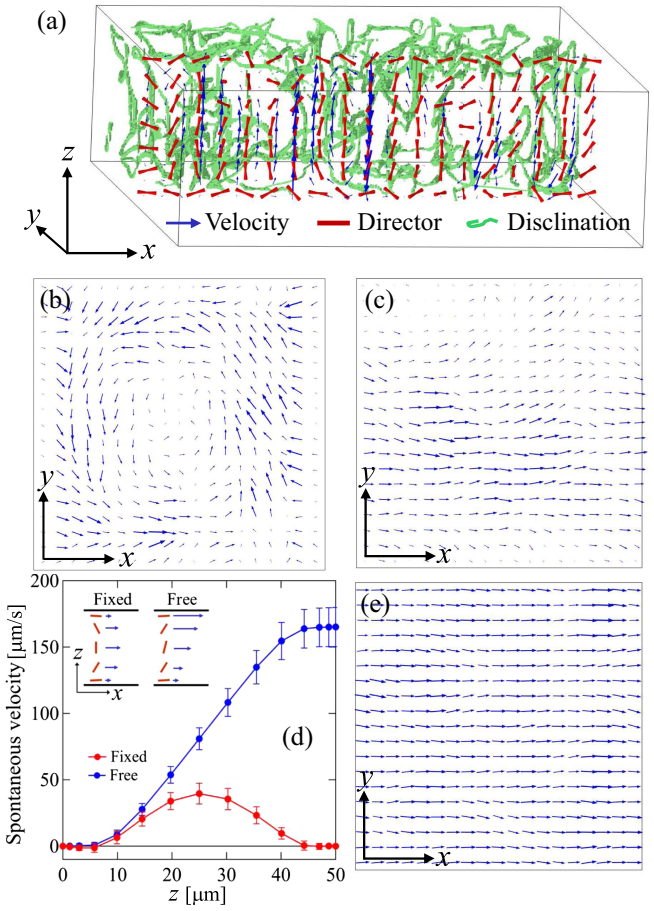


FIG. 4. Q-tensor-based 3D simulation results in steady DSM2 state. (a) Velocity (blue arrows), director (red rods) fields, and disclinations (green lines) ($E = 0.64$ V/μm; $f = 100$ Hz). (b) Mean velocity field of (a), averaged over a duration of 3.5 s on the midplane ($z = 25$ μm). (c) Mean velocity field with periodic boundary conditions imposed on the side boundaries perpendicular to the x axis. (d) z dependences of the velocity along the x axis, averaged over the x-y plane at each height z under fixed (red line) and free (blue line) conditions. Inset: schematic illustration of the macroscopic director (brown rods) and the mean velocity field (blue arrows). (e) Mean velocity field with the upper plate free to move in the x direction and periodic boundary conditions imposed on all side boundaries. See Supplemental Video4 [26] for the details of (a), and Supplemental Material (S3) [26] for the detail of the director field of (d).

present experimental results. The governing equations, derived from a variational principle [35], were solved using the finite-element method. The size of the electrode was set to 150×150 μm^2, as dictated by computational constraints. This size is much smaller than that of the 1.2×1.2 mm^2 experimental cell but is sufficient for qualitative comparison. Details of the simulation, including the equations and material parameters employed, are provided in Supplemental Material (S2) [26].

Figure 4(a) shows the simulation results in the steady state at $E = 0.64$ V/μm. As boundary conditions, the velocity was set to zero on all boundaries, while the director was fixed along the x direction. The velocity field, director field, and disclinations observed in Fig. 4(a) are all strongly disordered. Time-averaging over 3.5 s on the midplane ($z = 25$ μm) reveals a vortex structure [Fig. 4(b)], confirming spontaneous mean flow. Furthermore, when periodic boundary conditions are imposed on the two side boundaries perpendicular to the x axis, flow develops along the x direction [Fig. 4(c)]. The reduction in the flow velocity near the boundaries perpendicular to the y axis reflects the no-slip conditions at those surfaces. Figure 4(d) (red line) shows the z dependence of the mean x velocity, obtained by averaging over the regions $0\ \mu\text{m} < x < 150\ \mu\text{m}$ and $50\ \mu\text{m} < y < 100\ \mu\text{m}$, with a time interval of 3 s. The resulting profile is Poiseuille-like but differs in that the velocity gradient vanishes at the interfaces. This is a direct consequence of the absence of an applied pressure gradient, meaning that the shear stress at the interface is nil. Taken together, these results demonstrate that the boundary conditions govern the character of the spontaneous mean flow. Finally, Fig. 4(e) shows the velocity field on the midplane ($z = 25$ μm), averaged over 5 s, for the corresponding torque-free configuration, in which the upper plate is allowed to move freely in the x direction; periodic boundary conditions are also imposed on the side boundaries perpendicular to the y axis [17]. Again, flow develops in the x direction. Unlike the case with the fixed plate, the upper interface moves with a finite velocity, as shown by the blue line in Fig. 4(d). These results confirm that different mean flow regimes emerge depending on whether the upper plate is fixed or free to move. Furthermore, the inset of Fig. 4(d) demonstrates that the director field remains strongly correlated with the velocity field even in the turbulent state; see Supplemental Material (S3) [26] for details. It shows the depth dependence of the eigenvector corresponding to the largest eigenvalue of the Q tensor averaged over the x-y plane and over time, using the same averaging procedure as for the velocity field. We refer to this eigenvector as the *macroscopic director* (brown rods). Under the fixed boundary condition, the direction of the director tilt is opposite in the upper and lower halves of the cell, corresponding to the sense of the shear flow.

Although the three-dimensional simulations reproduce the formation of vortices, because of the limited aspect ratio of the simulation domain, the transient merging process observed in Fig. 2 could not be captured. To address this, simulations were performed for a larger system using a two-dimensional model that incorporates spontaneous flow [36], governed by

$$\rho\left(\frac{\partial}{\partial t} + \mathbf{v}\cdot\nabla\right)\mathbf{v} = a\left(v_0^2 - |\mathbf{v}|^2\right)\mathbf{v} - \nabla p + \eta\Delta\mathbf{v}, \quad (1)$$

where $\mathbf{v}$ and p are the two-dimensional velocity and pressure, and ρ and η denote the two-dimensional mass density and viscosity, respectively. In the full three-dimensional system, the time-averaged velocity profile across the cell thickness is approximately Poiseuille-like. The flow can therefore be characterized by the mean velocity at the cell midplane. Accordingly, the velocity in the present two-dimensional model is interpreted as the mean velocity at the midplane of the corresponding three-dimensional cell. Therefore, the present two-dimensional model is applicable only when a spontaneous flow has been established. The first term on the right-hand side, with $a > 0$, drives the velocity toward the characteristic spontaneous-flow speed v_0 [36]. The isotropic character of this equation is consistent with the experimentally observed absence of a preferred flow direction (Fig. 2) and with the three-dimensional simulation results [17]. By introducing the characteristic length $l_0 = \sqrt{\eta}/(\sqrt{a}v_0)$, corresponding to the vortex-core size, and the characteristic time $t_0 = \rho/(av_0^2)$, corresponding to the time required for the velocity to diffuse over a distance l_0, and scaling the length, time, and velocity by l_0, t_0, and v_0, respectively, Eq. (1) can be rewritten in dimensionless form with a single dimensionless parameter, $\mathrm{Re} = \rho/\sqrt{a\eta}$, corresponding to the Reynolds number based on the vortex-core size. In the following, all simulation results are presented in terms of these dimensionless variables. Details of the simulation procedure are provided in Supplemental Material (S4) [26].

Figure 5 shows the time evolution of the velocity field and the vorticity for $\mathrm{Re} = 1.5$ after the completion of small-vortex generation. The NLC region has a size of 40×40, and is surrounded by a layer of width 4 in which spontaneous flow is absent. To generate the initial small vortices, a random force is applied only during the interval $0 \le t \le 2$. The resulting vortices merge over time, eventually forming a single LSV, in good agreement with the experimentally observed formation process (Fig. 2). It should also be noted that the four vorticity arms extending from the center of the LSV are slightly twisted. The same feature is observed experimentally in Fig. 1(c). This twisting is associated with the Reynolds number; it disappears in the limit $\mathrm{Re} = 0$; see Supplemental Material (S4) [26].

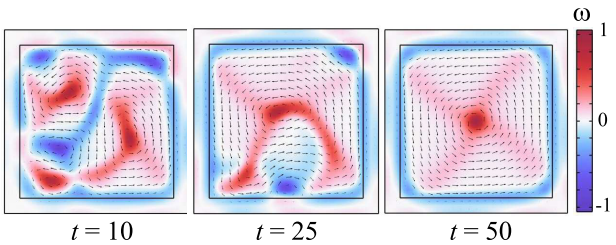


FIG. 5. 2D simulation results for LSV formation. Time evolution of velocity (arrows) and vorticity (color graduation) fields obtained from simulations, corresponding to the formation process of the LSV shown in Fig. 2. The system consists of inner and outer regions with and without an electric field; the boundaries are indicated by closed lines. See Supplemental Video 5 [26] for the details.

In summary, over 50 years after the discovery of dynamic scattering mode turbulence [13–15,20–22], this study reveals a cooperative mean flow hidden within this turbulent state, which has long been regarded as the ultimate form of disorder. The mean flow generates a large-scale vortex spanning the entire electrode area. Three-dimensional simulations reproduce these phenomena and reveal that vortex formation strongly depends on the boundary conditions. The flow field exhibits a Poiseuille-like profile in the bulk, where the velocity gradient vanishes at both interfaces, a distinctive property of this system. This behavior corresponds to the shear flow observed when the upper plate is free to move, i.e., under zero external shear stress [1–3]. In that case, the flow is also essentially simple shear in the interior but exhibits a zero velocity gradient at the interfaces. Previous simulations for such systems have shown that the flow field is correlated with the director field, suggesting that a positive feedback between these fields may lead to spontaneous shear flow [17]. A similar mechanism may also be relevant in the present cell with a fixed upper plate. The observed electrohydrodynamic turbulence shares key features with active nematic turbulence, in which internally generated stresses drive defect-mediated chaotic flows and mesoscale vortices in biological and synthetic systems [31,37–40]. In such systems, orientational distortions generate hydrodynamic stresses that destabilize the quiescent state and induce spontaneous flows. From this perspective, DSM2 turbulence is an electrically driven form of active nematic turbulence in which distortions of the director field break the spatial homogeneity, generate space charges through conductivity anisotropy, and drive flow via their interaction with the applied electric field. This mechanism is known as liquid-crystal-enabled electro-osmosis [41]. A key distinction from previously studied active turbulent systems is that active nematics do not, to the best of our knowledge, exhibit a persistent mean flow emerging from the turbulent state [18,19]. In contrast, the DSM2 state displays a clear and robust zero-wave-number spontaneous mean flow in the high-electric-field regime. Moreover, although large-scale flow organization has been reported in other turbulent systems, such as Rayleigh-Bénard convection [42] and parity-breaking fluids with odd viscosity [43], these structures are typically associated with finite characteristic wavelengths. Although confinement-induced macroscopic vortices have also been reported in active nematics [44], they do not emerge from a fully developed turbulent state. Nevertheless, DSM2 turbulence exhibits a system-spanning mean flow that emerges directly from defect-mediated turbulence. Future work should clarify how spontaneous LSV formation and its threshold depend on the cell

thickness, electrode domain size, aspect ratio, and NLC alignment conditions. These results establish a direct connection between electrohydrodynamic turbulence in liquid crystals and active nematic turbulence in biological and synthetic matter.

Acknowledgments—This work was supported by JSPS KAKENHI Grants No. 20K03872, No. 23K22461, and No. 25K07169, Izumi Science and Technology Foundation (No. 2020-J-017), Mazda Foundation (No. 20KK-084), and the Murata Science and Education Foundation (No. M24AN008).

Yuk. S., T. M., F. K., J. T., K. Y., Yuj. S., and T. N. performed experiments and analyses. H. O. and T. N. performed simulations. H. O., T. N., and J.-H. H. designed the project. J.-H. H., T. N., and H. O. wrote the manuscript. All authors have read and approved the final manuscript.

Data availability—There are no publicly available research data or software supporting this manuscript. Requests for further information or data should be sent to the authors.

[1] H. Orihara, Y. Harada, F. Kobayashi, Y.Sasaki, S. Fujii, Y. Satou, Y. Goto, and T. Nagaya, Negative viscosity of a liquid crystal in the presence of turbulence, Phys. Rev. E **99**, 012701 (2019).
[2] F. Kobayashi, Y. Sasaki, S. Fujii, H. Orihara, and T. Nagaya, Negative viscosity of liquid crystals in the presence of turbulence: Conductivity dependence, phase diagram, and self-oscillation, Phys. Rev. E **101**, 022702 (2020).
[3] T. Nagaya, T. Mera, S. Ujiie, F. Kobayashi, J.-H. Huh, and H. Orihara, A chemically robust fluorinated nematic liquid crystal exhibiting large negative apparent viscosity, J. Phys. Soc. Jpn. **95**, 054601 (2026).
[4] D. Saintillan, Rheology of active fluids, Annu. Rev. Fluid Mech. **50**, 563 (2018).
[5] A. Lanzaro and L. Gentile, Rheology of active fluids, In *Out-of-Equilibrium Soft Matter: Active Fluids*, edited by C. Kurzthaler, L. Gentile, and H. A. Stone (Royal Society of Chemistry, London, 2023).
[6] H. M. López, J. Gachelin, C. Douarche, H. Auradou, and E. Clement, Turning bacteria suspensions into superfluids, Phys. Rev. Lett. **115**, 028301 (2015).
[7] A. Sokolov and I. S. Aranson, Reduction of viscosity in suspension of swimming bacteria, Phys. Rev. Lett. **103**, 148101 (2009).
[8] A. Loisy, J. Eggers, and T. B. Liverpool, Active suspensions have nonmonotonic flow curves and multiple mechanical equilibria, Phys. Rev. Lett. **121**, 018001 (2018).
[9] P. G. de Gennes and J. Prost, *The Physics of Liquid Crystals*, 2nd ed. (Oxford University Press, Oxford, New York, 1993).
[10] R. Williams, Domains in liquid crystals, J. Chem. Phys. **39**, 384 (1963).
[11] E. F. Carr, Influence of electric fields on the molecular alignment in the liquid crystal p-(anisalamino)-phenyl acetate, Mol. Cryst. Liq. Cryst. **7**, 253 (1969).
[12] W. Helfrich, Conduction-induced alignment of nematic liquid crystals: Basic model and stability considerations, J. Chem. Phys. **51**, 4092 (1969).
[13] S. Kai and W. Zimmermann, Pattern dynamics in the electrohydrodynamics of nematic liquid crystals, Prog. Theor. Phys. Suppl. **99**, 458 (1989).
[14] N. Eber, P. Salamon, and A. Buka, Electrically induced patterns in nematics and how to avoid them, Liq. Cryst. Rev. **4**, 101 (2016).
[15] J.-H. Huh and H. Osoguchi, Formation of grid patterns in an ac-driven electroconvection system, Phys. Rev. E **101**, 062701 (2020).
[16] M. C. Cross and P. C. Hohenberg, Pattern formation outside of equilibrium, Rev. Mod. Phys. **65**, 851 (1993).
[17] H. Orihara and T. Nagaya, Simulations of electric-field-induced turbulence and negative viscosity in conductive nematic liquid crystals, Phys. Rev. E **112**, 065406 (2025).
[18] M. Serra, L. Lemma, L. Giomi, Z. Dogic, and L. Mahadevan, Defect-mediated dynamics of coherent structures in active nematics, Nat. Phys. **19**, 1355 (2023).
[19] L. C. Head, C. Doré, R. R. Keogh, L. Bonn, G. Negro, D. Marenduzzo, A. Doostmohammadi, K. Thijssen, T. López-León, and T. N. Shendruk, Spontaneous self-constraint in active nematic flows, Nat. Phys. **20**, 492 (2024).
[20] S. Kai, W. Zimmermann, M. Andoh, and N. Chizumi, Local transition to turbulence in electrohydrodynamic convection, Phys. Rev. Lett. **64**, 1111 (1990).
[21] H. Kawamoto, The history of liquid-crystal displays, Proc. IEEE **90**, 460 (2002).
[22] K. A. Takeuchi, M. Kuroda, H. Chate, and M. Sano, Directed percolation criticality in turbulent liquid crystals, Phys. Rev. Lett. **99**, 234503 (2007).
[23] J.-H. Huh, Y. Hidaka, A. G. Rossberg, and S. Kai, Pattern formation of chevrons in the conduction regime in homeotropically aligned liquid crystals, Phys. Rev. E **61**, 2769 (2000).
[24] W. Thielicke and E. J. Stamhuis, PIVLab: Towards user-friendly, affordable and accurate digital particle image velocimetry in MATLAB, J. Open Res. Software **2**, e30 (2014).
[25] W. Thielicke and R. Sonntag, Particle image velocimetry for MATLAB: Accuracy and enhanced algorithms in PIVLab, J. Open Res. Software **9**, 12 (2021).
[26] See Supplemental Material at http://link.aps.org/supplemental/10.1103/rh1y-bsjj for additional details on the experimental methods, data analysis, and numerical simulations; Supplemental Video1 shows the time evolution of the velocity field (arrows) and vorticity field (color scale), corresponding to Fig. 1(b). The displayed time interval is $t = 0.3$–1.5 s; Supplemental Video2 shows the time evolution of the velocity field (arrows) and vorticity field (color scale), corresponding to Fig. 2. The displayed time interval is 0.85 s; Supplemental Video3 shows the actual motion of micro-pearls in the DSM2 state, recorded at 200 frames per second; Supplemental Video4 shows the time evolution of the director field (red rods) and velocity field (blue arrows) over 1 s in the steady state, corresponding to Fig. 4(a). The

video is shown in slow motion for clarity; Supplemental Video5 shows the time evolution of the velocity field (arrows) and vorticity field (color scale) from the 2D simulation, shown over the time interval $t = 0$–50.

[27] A. Joets and R. Ribotta, Localized, time-dependent state in the convection of a nematic liquid crystal, Phys. Rev. Lett. **60**, 2164 (1988).

[28] M. Dennin, G. Ahlers, and D. S. Cannell, Chaotic localized states near the onset of electroconvection, Phys. Rev. Lett. **77**, 2475 (1996).

[29] J.-H. Huh, Traveling waves and worms in ac-driven electroconvection under external multiplicative noise, Phys. Rev. E **95**, 042704 (2017).

[30] A. de Lózar, W. Schopf, I. Rehberg, D. Svensek, and L. Kramer, Transformation from walls to disclination lines: Statics and dynamics of the pincement transition, Phys. Rev. E **72**, 051713 (2005).

[31] T. N. Shendruk, K. Thijssen, J. M. Yeomans, and A. Doostmohammadi, Twist-induced crossover from 2D to 3D turbulence in active nematics, Phys. Rev. E **98**, 010601(R) (2018).

[32] T. W. Stinson, III, and J. D. Litster, Pretransitional phenomena in the isotropic phase of a nematic liquid crystal, Phys. Rev. Lett. **25**, 503 (1970).

[33] C. Zannoni, Liquid crystal observables: Static and dynamic properties, in *Advances in the Computer Simulations of Liquid Crystals*, edited by P. Pasini and C. Zannoni (Springer Dordrecht, Dordrecht, 1999).

[34] E. Bodenschatz, W. Zimmermann, and L. Kramer, On electrically driven pattern-forming instabilities in planar nematics, J. Phys. (Les Ulis, Fr.) **49**, 1875 (1988).

[35] O. M. Tovkach, C. Conklin, M. C. Calderer, D. Golovaty, O. D. Lavrentovich, J. Vinals, and N. J. Walkington, Q-tensor model for electrokinetics in nematic liquid crystals, Phys. Rev. Fluids **2**, 053302 (2017).

[36] J. Toner and Y. Tu, Flocks, herds, and schools: A quantitative theory of flocking, Phys. Rev. E **58**, 4828 (1998).

[37] T. Sanchez, D. T. N. Chen, S. J. DeCamp, M. Heymann, and Z. Dogic, Spontaneous motion in hierarchically assembled active matter, Nature (London) **491**, 431 (2012).

[38] H. H. Wensink, J. Dunkel, S. Heidenreich, K. Drescher, R. E. Goldstein, H. Löwen, and J. M. Yeomans, Meso-scale turbulence in living fluids, Proc. Natl. Acad. Sci. U.S.A. **109**, 14308 (2012).

[39] A. Doostmohammadi, J. Ignés-Mullol, J. M. Yeomans, and F. Sagués, Active nematics, Nat. Commun. **9**, 3246 (2018).

[40] R. Alert, J. Casademunt, and J.-F. Joanny, Active turbulence, Annu. Rev. Condens. Matter Phys. **13**, 143 (2022).

[41] I. Lazo, C. Peng, J. Xiang, S. V. Shiyanovskii, and O. D. Lavrentovich, Liquid crystal enabled electro-osmosis through spatial charge separation in distorted regions as a novel mechanism of electrokinetics, Nat. Commun. **5**, 5033 (2014).

[42] A. Pandey, J. D. Scheel, and J. Schumacher, Turbulent superstructures in Rayleigh–Bénard convection, Nat. Commun. **9**, 2118 (2018).

[43] X. M. de Wit, M. Fruchart, T. Khain, F. Toschi, and V. Vitelli, Pattern formation by turbulent cascades, Nature (London) **627**, 515 (2024).

[44] H. Wioland, F. G. Woodhouse, J. Dunkel, J. O. Kessler, and R. E. Goldstein, Confinement stabilizes a bacterial suspension into a spiral vortex, Phys. Rev. Lett. **110**, 268102 (2013).